RESEARCH ARTICLE

N-doped carbon nanotube sponges and their excellent lithium storage performances

Qi Zhu[1] | Andrés R. Botello-Méndez[2] | Luhua Cheng[1] | Juan Fajardo-Diaz[3] |
Emilio Muñoz-Sandoval[3] | Florentino López-Urias[3] | Jiande Wang[1] |
Jean-François Gohy[1] | Jean-Christophe Charlier[1] | Alexandru Vlad[1] (ORCID)

[1] Institute of Condensed Matter and Nanosciences, Université catholique de Louvain, Louvain-la-Neuve, Belgium

[2] Departamento de Física Química. Instituto de Física, Universidad Nacional Autónoma de México, Mexico

[3] Advanced Materials Division, IPICYT, San Luis Potosí, Mexico

Correspondence
Alexandru Vlad, Institute of Condensed Matter and Nanosciences, Université catholique de Louvain, Louvain-la-Neuve, Belgium.
Email: alexandru.vlad@uclouvain.be

Funding information
CF-ARC, Grant/Award Number: 18/23-093; CONACYT for Grant Problemas Nacionales, Grant/Award Number: 2016-1-4148

Abstract

Preparation, analysis and lithium storage performance of a series of nitrogen-doped carbon nanotube sponges (CNX) is presented in this work. The synthesis was performed using an aerosol-assisted chemical vapor deposition (AACVD) in a bi-sprayer system by using various carbon and nitrogen precursors made of mixtures of benzylamine with toluene, urea, pyridine and 1,2-dichlorbenzene, with ferrocene as catalyst. A series of physico-chemical analysis techniques are used to characterize the composition and the morphology of the obtained materials, and a correlation of these with the lithium storage performances is attempted. The samples reveal an interconnected core-shell CNX fiber morphology with a CNT-core surrounded by an amorphous carbon shell. Appealing lithium storage performances are attained, while also considering aspects of safety, low potential, and long-term cycling stability. The best performing sponges display a high specific capacity (223 mAh g^{-1}) when cycled in a practically relevant voltage window (0.01–1V vs. Li), high first cycle (90%) and long-term cycling (99.3%) coulombic efficiencies and excellent capacity retention after 1500 cycles. This study further analyses the interplay between the morphology and the physico-chemistry of nitrogen-doped carbon nanotube materials for Lithium storage and provides guidelines for future developments.

KEYWORDS
CNT sponge, ferrocene catalyst, lithium storage, nitrogen doping

1 | INTRODUCTION

The rapidly evolving market of electrically powered vehicles and portable electronics drives a great demand for electrochemical energy storage devices with enhanced performances. Lithium-ion batteries (LIBs) exhibit plenty of advantages, including high gravimetric/volumetric capacities, power density, long lifespan and start attaining practically appealing cost metrics.[1–3] Ever since Sony Co. commercialized the world's first LIBs with a

tailor-made carbon negative electrode,[4] great efforts have been devoted to exploring novel energy storage materials.[5–20] Graphite is commonplace among commercial LIBs because of low redox potential, good stability and electrical conductivity. The electrochemical de/lithiation process, known as de/intercalation, is the mechanism through which graphite is able to store lithium.[21]

Whilst graphite anodes have dominated the market share of LIBs, other carbon materials have been investigated, including soft and hard carbon,[22] graphene[23] as well as other carbon allotropes.[24] Carbon nanotubes (CNTs) have been considered as an alternative for anode material for lithium batteries,[25,26] owing to the property of lightweight, good chemical stability, large surface area as well as relatively higher redox potential avoiding the close to Li-plating limit of graphite, when especially used at high current densities. CNTs also exhibit high room-temperature electrical conductivities, in the order of 100 S m^{-1}, large tensile strength of up to 60 GPa, high rigidity, and low density.[27] However, the disadvantages of CNTs are their 1D morphology, low compaction density, as well as need of improvement of large-scale production methods. In addition, characteristics of CNTs such as diameter, number of layers, length, defect density, and electronic properties, are also considered as important factors that need to be take into account for the development of reliable CNTs lithium-based anodes.[28]

Another issue with the use of CNTs in LIBs is the irreversible first-cycle capacity due to excessive solid electrolyte interphase (SEI) formation. Although this phenomenon is also characteristic for other carbon materials, the problem is more pronounced in carbon nanotubes given their high specific surface area. Additionally, a practically relevant problem for lithium storage in CNTs is the absence of a voltage plateau during lithiation/delithiation.[29] This can make troublesome the use CNT based LIBs in applications requiring a stable voltage supply, yet advantageous for high-power cells as Li-plating voltage range can be avoided. Finally, 3D crosslinked CNTs architectures are preferred to satisfy the safety requirements while working with nanomaterials and to increase the compaction density of the active material within the electrode.[30] Carbon nanotube sponges (CNX), as a typical three-dimensional tubular structure, have thus attracted much attention in recent years.[31–33]

The chemical doping in carbon nanostructures has been shown efficient to alter the chemical reactivity, photophysical properties, electrical conductivity, as well as the electrochemical performances.[34,35] Nitrogen and boron are ideal prospects to dope carbon materials because they both are neighboring atoms in the periodic table, have a similar atomic radius to that of the carbon and can covalently bind to carbon.[36] It has been shown that doping of mul-

tiwalled CNTs with boron induces acceptor states near the valence band edge.[37] Instead, nitrogen has five electrons in its valence band and acts as an electron donor, producing carbon nanostructures with a metallic behavior. Nitrogen-doped carbon materials have thus shown enhanced electrocatalytic activity for the oxygen reduction reaction (ORR),[38] attributed first to the increase of edge reactivity, promoting the creation of active sites for chemisorption of oxygen and nitrogen-originating surface groups.[39] Introducing heteroatoms (such as boron or nitrogen atoms) into the carbon nanotube structures has proven to be a very effective way to enhance the reactivity and electrical conductivity, as nitrogen can provide additional free electrons for the conduction band, hence increase the Li$^+$ ion storage rate capabilities.[40] Based on these factors, novel CNT sponges with different nitrogen dopants (CNXs) are desirable for Li$^+$ ion storage.[41–43]

In this work, we present the synthesis of CNXs (nitrogen-doped CNX) by using different carbon/nitrogen precursors filled into two separate sprayers, with the method of aerosol-assisted chemical vapor deposition (AACVD). Benzylamine (BZ)-toluene, BZ-urea, BZ-pyridine, BZ-1,2-dichlorbenzene (with addition of 2.5 wt.% ferrocene as catalyst) and BZ-1,2-dichlorbenzene (with addition of 12 wt.% ferrocene as catalyst) were used as carbon and nitrogen dopant sources, respectively. Our previous work has shown the complex behavior during the growth with the carbon and the nitrogen precursor playing an essential role on morphology, surface nitrogen concentration, as well the types of functional groups present at the surface.[44] When utilized as anodes in LIBs, these CNX sponges present excellent capacity and rate capability, in particular when operated in a narrow potential range of practical relevance between 0.01–1 V (vs. Li$^+$/Li^0). We further analyze the correlation between the composition, physico-chemical and lithium storage properties of the studied CNX materials. Despite the significative differences in chemical and structural composition, moderate differences are found in the electrochemical responses, and in particular in attained specific capacities, and capacity retention. First cycle, and continuous cycling columbic efficiencies are however found to be different, significative of SEI growth and stability dynamics, assigned to different surface functionalities and fiber morphologies.

2 | RESULTS AND DISCUSSION

The morphology and structure of CNXs were first investigated by scanning electron microscopy (SEM, Figure 1A--E and S1) and transmission electron microscopy (TEM, Figure S2). The 3D CNX sponges consist of randomly

FIGURE 1 Morphology characterization of CNXs materials studied in this work. A–E, SEM images of CNX1 to CNX5 samples, respectively. H, XRD patterns of CNX1–CNX5 highlighting the asymmetric C(002) peak
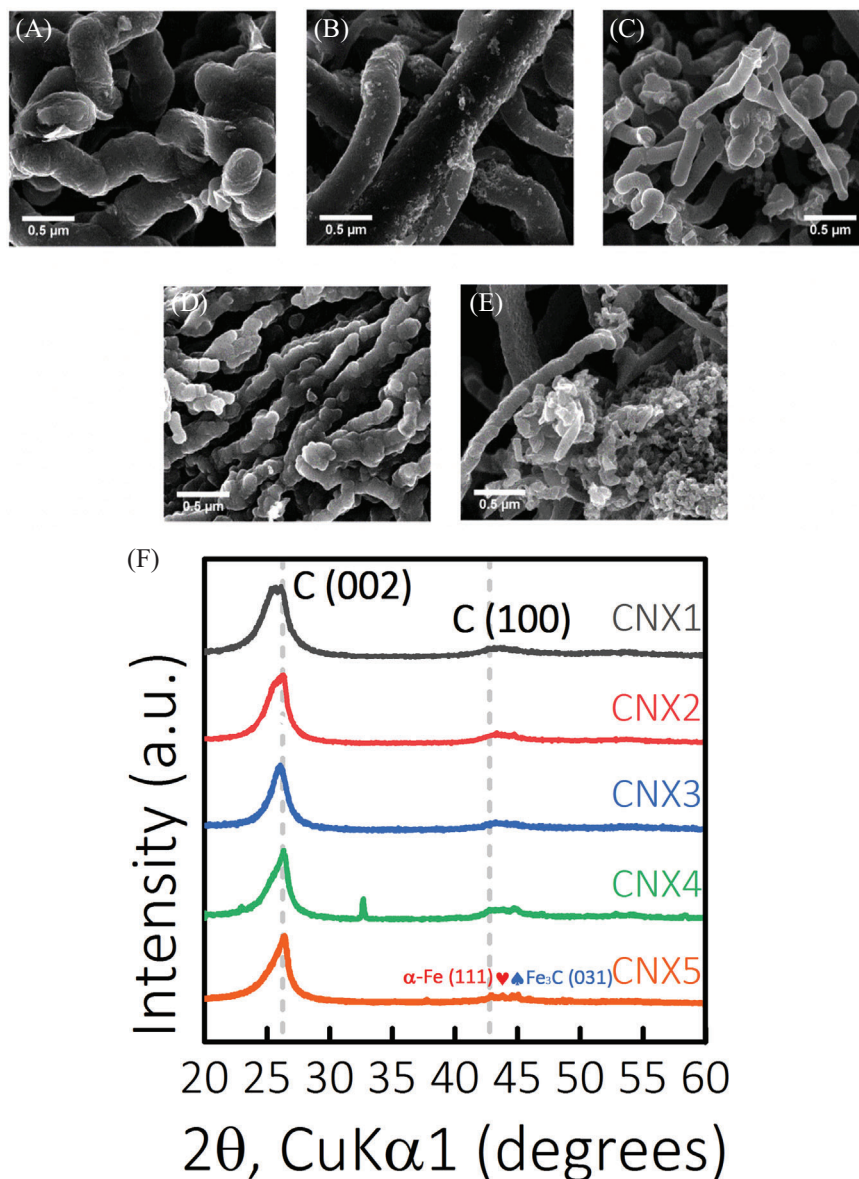
oriented and entangled carbon tubes, and are composed of a graphitic MWCNT core, surrounded by an amorphous/disordered carbon shell (as proved by TEM analysis and previously reported structural analysis[44]). Different sizes and tubular aspects at low magnification are shown in Figure S1. The main carbon/nitrogen precursor source, benzylamine, favors the entangled corrugated carbon fibers.[44,45] Different morphologies and tube size observed in Figure 1 are attributed to different carbon/nitrogen precursor used.[44] Figure 1A, corresponding to typical CNX1 morphology, shows a twined and bended morphology. The uniform sizes relate to the toluene precursor, which serves as the carbon source for nanotube growth.[46] The use of urea (CNX2, Figure 1B) as the precursor, leads to the growth of less curved (straight) tubes, whilst also decomposing to NH_3 and HNCO at the high growth temperatures that can affect the composition, doping levels, as well as the

morphology. CNX3 tubes (Figure 1C) exhibit much smaller diameter than CNX1 and CNX2, since the pyridine-based precursors favor entanglement of CNTs during growth.[44] CNX4 and CNX5 display similar morphologies with similar tube diameters as for CNX3, however displaying much corrugated surface morphology. The combination of dichlorobenzene/ferrocene is more favorable for forming Fe-filled carbon nanotubes and CNX5 formed the densest structure, probably due to the high-level of ferrocene used.

Morphological analysis and comparisons, although displaying some differences between the prepared samples, cannot identify the properties of the CNXs and a number of complementary techniques were carried out. To analyze the crystallinity of the studied CNX materials, powder XRD analysis was performed and the data are shown in Figure 1F. All CNXs displayed a major diffraction peak at 26° that corresponds to the (002) Miller index from the
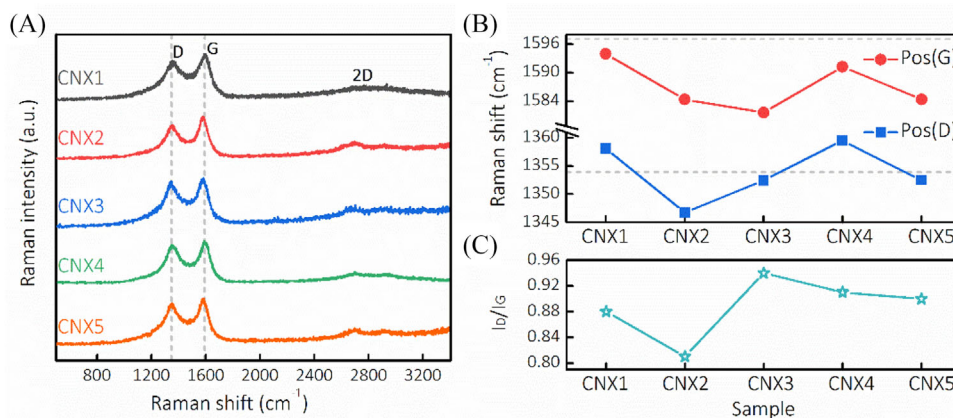
FIGURE 2 A, Full Raman spectra of CNX samples studied in this work. B, Raman shifts for D and G bands and (C), the ratio of D and G band (I_D/I_G). In (B), the two dotted horizontal lines correspond to position of D and G bands in graphite, and are used as eye guide line

stacking of graphene layers, and a weak and broadened (100) peak characteristic of disordered carbon layers.[47] The signal around $2\theta = 44°$ is be associated with Fe_3C (PDF Card: 00-043-0001) and α-Fe (PDF Card: 00-006-0696). The shift of the C(002) diffraction peak suggests higher disorder, or more amorphous phases in the order from CNX1 to CNX5.[48]

The structure of CNXs was next examined using Raman spectroscopy. As Figure 2A shows, the Raman spectra of CNX1–CNX5 samples presents two prominent peaks in the range of 1350–1600 cm^{-1}. These peaks are characteristic of graphitic materials: the D band is correlated with disordered and defective graphitic layers, whereas the G band corresponds to the stretching of C-C bonds in graphitic materials. The ratio of intensities of disordered (I(D)) to ordered (I(G)) carbon can quantitatively describe the degree of disorder. The low intensity of 2D band observed at around 2700 cm^{-1}, is related to the number of the graphitic layers.

Despite the similarity of the Raman plots, it is possible to detect changes in the band shift and the intensity for I_D/I_G ratio of different peaks, which can be linked to the crystallinity of the carbon fiber. The analysis of the Raman shifts for the D and G bands is shown in Figure 2B. Compared with the graphite G-peak (1581 cm^{-1}), the G band for all studied CNXs exhibit an upshift, assigned to nitrogen doping and defects.[49] For the position of the D-peak, when compared to that of graphite (1354 cm^{-1}) the correlation is less straightforward. The upshift (as observed for CNX1 and CNX4) can be related to the compression of graphite layers, whereas the downshift (as observed for CNX2, CNX3 and CNX5) could be correlated to the expansion of the C-C bonds.[50] The intensity ratio of D band and G band (I_D/I_G) can be related to a combined effect of ordering degree and nitrogen doping content.[51] As shown in Figure 2C, values of $I_D/I_G < 1$ indicate that CNXs are also

composed of ordered graphites. Among all the samples, CNX3 ($\sim$0.94) gives the highest value of I_D/I_G whereas CNX2 exhibits the lowest ($\sim$0.81). Although some have correlated this directly to nitrogen content, the XPS surface composition analysis discussed in the following does not supports this, implying either surface-bulk segregation of nitrogen dopant species, or combined effect of disorder.

In order to assess the thermal stability of the CNX phases, TGA was carried. The TGA profile of all CNXs samples is presented in Figure 3A, and offer the residual mass percentages of CNXs. CNX5 has the highest residue ($\sim$3.8%) whereas CNX1 and CNX4 give the lowest ($\sim$1.6%). Overall, a low calcination residue is left, and the attained values (within the experimental error) can be assigned to various catalyst content left from the synthesis (e.g., highest for CNX5 given that 12,5 wt.% solution of ferrocene was used). Figure 3B shows the derivative weight loss (DTG) plot, which reflects the maximum weight loss rate of CNXs, or the oxidation (decomposition) temperature of the studied CNX samples. The thermal stability of CNXs follows the order CNX3 < CNX5 < CNX4 < CNX1 < CNX2; which correlates with the Raman $I_D:I_G$ ratio analysis (Figure 2) and can thus be correlated to the graphitization (disorder) degree of the analyzed CNX.

XPS was carried out to investigate the chemical species present in CNXs. The spectral-deconvolution of C 1s and O 1s are used to estimate the oxygen functional groups, whereas N 1s could offer evidence of the formation of nitrogen embedded in the graphitic layers. As shown in Figure 4, for all the CNXs, the main contribution to the XPS spectra is attributed to the strong C=C bonding (sp^2), manifesting the graphitic nature of the synthesized CNX. A minor presence of C—C, C=O/C—N and C—Fe bonds are also detected, which are caused by sp^3 hybridized carbons, ester/ethoxy groups and the presence of residual of iron carbide phases (Fe_3C, etc.), respectively.
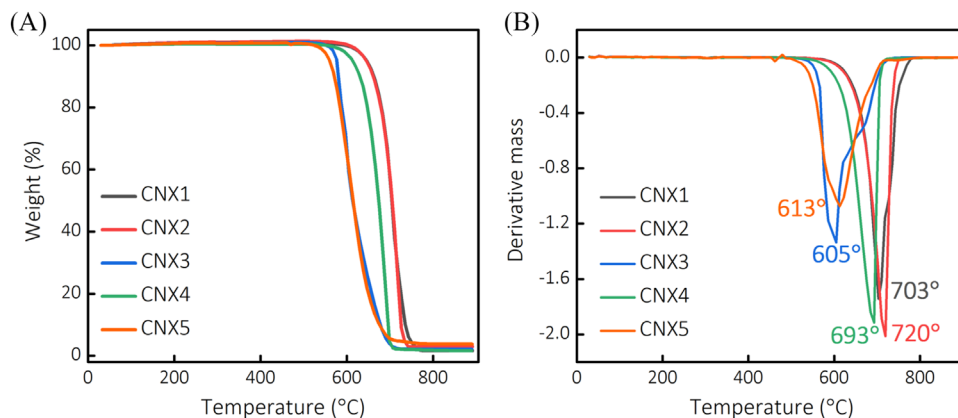
FIGURE 3 A, TGA analysis and (B) corresponding DTG of CNX samples analysed in this work
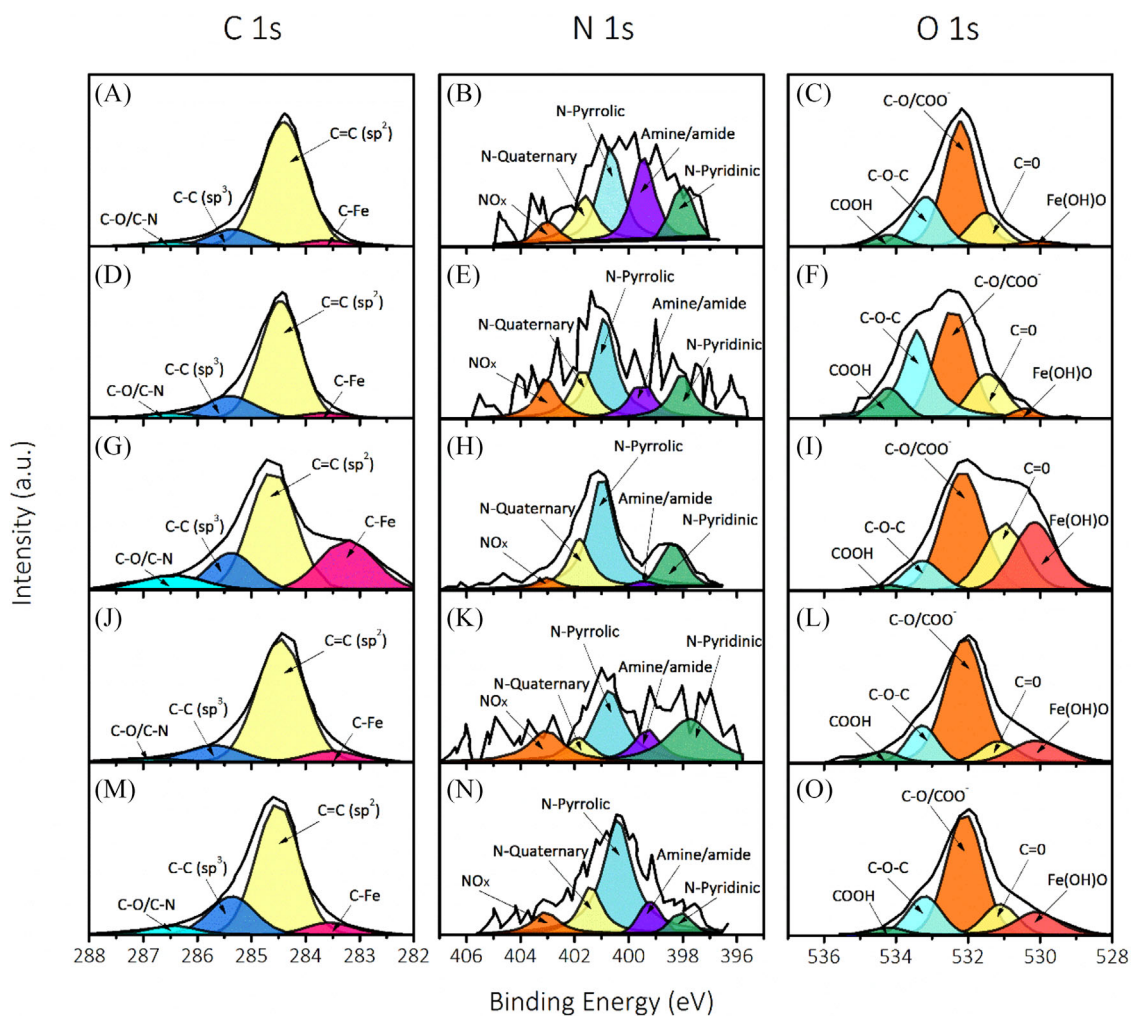
FIGURE 4 High-resolution XPS spectra for the C1s, N1s, and O1s core level. The results for the sample CNX1 (A–C), CNX2 (d-f), CNX3 (G–I), CNX4 (J–L) and CNX5 (M–O)

TABLE 1 Main surface atomic percentages for CNX1 to CNX5 samples, as determined from XPS analysis

Sample	% C	% O	% N	% Si	% Cl
CNX1	93.8	4.1	<0.1	2.1	N.D.
CNX2	94.9	2.8	2.3	N.D	N.D.
CNX3	87.0	8.3	3.0	1.7	N.D.
CNX4	93.0	5.7	<0.1	1.3	N.D.
CNX5	93.1	5.1	0.2	1.0	0.6

Note: N.D. stands for not detected

Abbreviation: CNX, carbon nanotube sponges.

The high-resolution N1s peaks can be deconvoluted into five components including N-pyridinic (398.7 eV), amine/amide (399.3 eV), N-pyrrolic (400.4 eV), N-Quaternary (401.9 eV), and NO_x (403.1 eV).[33] In general, N_{pyr}, N_{py} and N_Q doping are favored for all CNXs (especially for dominated N_{pyr}), which enhances the electronic conductivity of carbon matrices, thereby improving the electrochemical activity. Nitrogen precursors are also the dominant factors of the concentration of nitrogen functional groups as well as the carbon lattice. Analysis shows that CNX3 (Figure 4, Table 1) exhibits highest concentrations of surface oxygen and nitrogen species, CNX2,5 also have large amounts of surface nitrogen (with higher oxygen for CNX5); whereas CNX1,4 display high oxygen content, with low nitrogen amounts. As next discussed, a certain correlation is found between these with, for example the combination of high oxygen and nitrogen surface species resulting in highest coulombic efficiencies attained.[52] The spectral-deconvolution of O 1s signal indicates the presence of different type of oxygen functional groups and content. The signal of C—O—C, C—O/COO⁻ and C=O bonds is important in all CNXs samples, but particularly enhanced in CNX2 and CNX3. The presence of C=C, C=O and C—N groups is also confirmed from FTIR analysis (shown in Figure S3). Table 1 presents the main surface atomic percentages of CNX1–CNX5 samples. It is highly notable that the main contribution of nitrogen can be found in CNX2 and CNX3 samples when urea and pyridine are used, respectively. The CNX3 sample also has the highest surface oxygen content of all samples. It is worth to mention that CNX5 sample shows a perceptible amount of Chlorine atoms. Although CNX4 is prepared from similar precursors, higher content of ferrocene is used for CNX5, and higher Cl content could be due to fixation by Fe species remained in the sample.

To investigate the electrochemical properties of the CNXs samples, Li-half cells were assembled by employing pure CNXs electrodes (binder and additive free; rectangular sheets cut from as prepared samples) as the working electrodes. Electrochemical impedance spectroscopy (EIS)

was employed to evaluate the charge transfer efficiency of CNXs-based cells. Figure 5A displays the initial normalized EIS before cycling, whereas the EIS results after 50 and 100 cycles are shown in Figure S4a and b, respectively. The EIS contain a high-frequency semicircle and a low-frequency line. While the low-frequency line is attributed to the "Warburg impedance" resembling the diffusion of Li ions within the carbon nanotubes, the compressed semicircle is mainly attributed to the charge-transfer (R_{CT}) resistance at the electrode/electrolyte interface.[53] As shown in Figure 5A, the charge-transfer resistance of CNX3,5 cells are the lowest, that could be attributed to improved conductivity, given the higher nitrogen content (Figure 4), as well as disordered nature (as interpreted from Figures 2 and 3 analysis) of these samples. CNX2 has also a high nitrogen content, however the higher charge transfer resistance could be assigned to larger tube size and thus lower surface area (Figure 1B).

The rate capability results, as depicted in Figure 5B, reveal the performance of CNXs electrodes at various cycling rates from 0.25 to 10 C (wherein 1C rate corresponds to a current density of 200 mA g⁻¹). CNX5 displays the best rate performances, corroborating the improved charge transfer interface as also confirmed by EIS analysis. Other CNX display slightly lower rate performances, which could be assigned to complex interplay between the amorphous shell size, conductivity, dopants amount and homogeneity. Overall, CN2,3&5 are found to be the best performing in this series, corroborating as well the EIS data, and could be explained by the higher N-content and thus higher conductivity. The capacity retention at different C-rates is depicted in Figure 5C. At a cycling rate of 0.25 C, CNX5 delivers a capacity of 220 mAh g⁻¹. There is a gradual capacity reduction with the increasing rate, although 48 mAh g⁻¹ reversible capacity was maintained even at a high rate of 10 C. More importantly, CNX5 maintained its high and reversible capacity (211.4 mAh g⁻¹) after the variable C-rate test, which indicates a high stability of the Li-storage process in CNX5 sample.

The galvanostatic charge/discharge behavior of the five CNXs electrodes at a rate of 0.1 C (current density equals to 10 mA g⁻¹) was next evaluated (Figure S5) and the cycling performance is presented in Figure 5D. The working window potential range was set from 0.01–1V versus Li⁺/Li. The initial discharge capacities of CNX1–CNX5 are 206, 195, 216, 197 and 223 mAh g⁻¹, respectively. Although these figures may seem low when compared to other reports, it has been stressed out that these capacities are attained within a narrow potential window of 1V (0.01–1V vs. Li⁺/Li, Figure S5). First of all, this is considered as the practical working window for a negative electrode material of a Li-ion battery, as working at higher potentials will penalize the output voltage of a full cell. Furthermore,
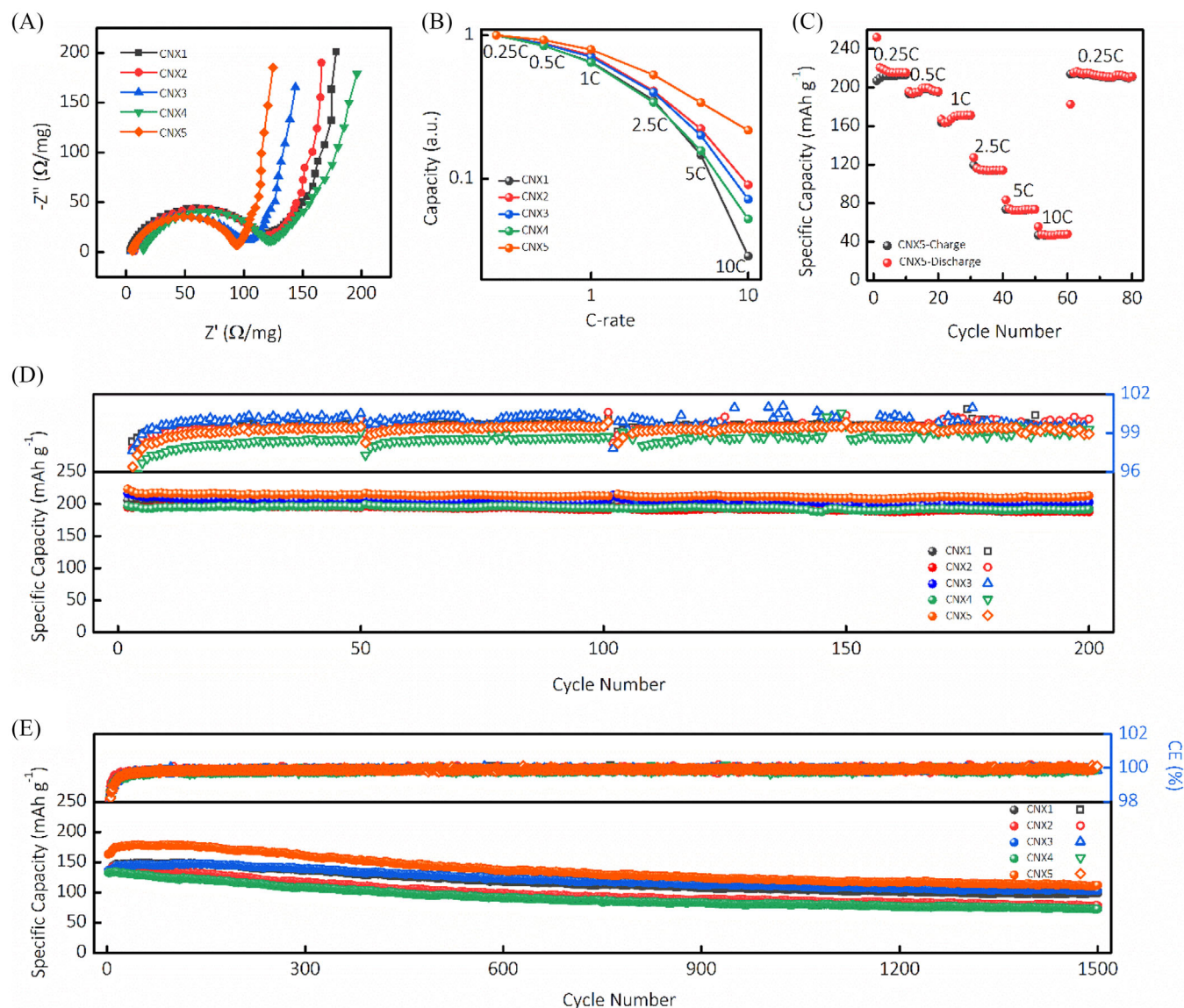
FIGURE 5 A, Normalized per mass of electrode electrochemical impedance spectroscopy (EIS) plots and (B) rate capability of CNX1–CNX5 samples. C, Capacity retention function of rate for CNX5 based electrodes. Cycling performance of CNX1–CNX5 at a cycling rate of C/10 (D) and of 1C (E). Top and bottom insets represent the coulombic efficiency and specific capacity retention with cycling, respectively

increasing the potential above 1V (vs. Li+/Li) results in SEI decomposition so that at the next cycles, additional SEI will be formed, leading to lower average coulombic efficiency and continuous consumption of the electrolyte.[54,55] And lastly, to be mentioned that contrary to lithium storage in many amorphous hard or soft carbons, a major capacity contribution for CNX samples is attained well above the 0V (vs. Li+/Li) limit where unsafe Li-metal plating can take place. As such, practically appealing storage performances are attained, if considering all aspects of safety, low potential, and long-term cycling stability.

After 200 cycles, all of CNXs are found to maintain an good and similar capacity retention with cycling.

The reversible capacities of CNX1–CNX5 are 193, 188, 203, 192and 213 mAh g^{-1}, respectively. Additionally, the coulombic efficiency was stabilized at around 99.3% after initial formation cycles. The long-term cycling stability CNXs was further investigated at a higher rate of 1 C (Figure 5E). The first discharge capacities of CNX1–CNX5 were corresponding to 136, 135, 137, 133 and 163 mAh g^{-1}, respectively. After 1500 cycles at 1 C, the capacity of CNX5 was able to retain at 112 mAh g^{-1}. The corresponding capacity retention was about 68.7%, representing an ultralow capacity decay of only 0.021% per cycle. Similarly, the other four CNXs exhibited analogous high-capacity retention (99, 78, 103 and 73 mAh g^{-1} for CNX1–CNX4, respectively). More

importantly, the corresponding coulombic efficiency of all five CNXs remained as high as 99.9% after 1500 cycles.

It is interesting to note that despite the noticeable variation in composition and morphology, there are less deviations in some lithium storage metrics. For instance, the specific capacities attained varied within a narrow range between 188 and 213 mAh g^{-1} Figure 5D). It can be thus considered that dopant content, surface chemistry, disorder, defects and CNX fiber morphology has limited impact on attainable Li-storage amounts. Power performances and charge transfer resistance (Figure 5A and 5B) are however found dependent on nitrogen content and fiber morphology, oppositely affecting the charge transfer efficiency and electrochemical surface area, respectively.[44] Finally, the coulombic efficiency during cycling, primarily affected by the surface chemistry, does not seem to directly correlate with measured N and O content, yet corroborates with the relative atomic ratio of carbonyl/carboxylate surface functions (Figure 4).[44] Highest efficiency averaged over the first 100 cycles is attained for CNX3 (Figure 5D), with O and N content of 8.3% and 3.0%, respectively; while lowest for CNX4, with O and N content of 5.7% and < 0.1%. The deconvolution of O 1s signal in XPS spectra indeed reveals higher COO$^-$/CO content of CNX3, followed CNX1,2, and lowest for CNX4,5. The averaged coulombic efficiency over the first 100 cycles indeed follows a similar trend (CNX3 > CNX1 > CNX2 > CNX5 > CNX4, Figure 4D-top) and is assigned to stability of SEI promoted by redox active surface carbonyl functions.[56]

The electrochemical analysis combined to physico-chemical and morphological characterization highlights the correlation of these for robust and stable lithium storage. The spongy cross-linked morphology is first of all shown to be beneficial for allowing pure CNX electrode fabrication (i.e.,—no binder and no additional additives required). The stability of the electrode during the preparations (e.g., cutting circular or square shaped electrodes directly from the as grown samples), but in particular stability with cycling highlights the benefits of having an inter-woven structure, where not only the mechanical properties are being exploited, but also the continuous electrical charge transport pathways for efficient electrochemical utilization. This may be further accentuated and important aspect for negative electrode materials wherein the SEI formation can lead to growth of electrically insulating films between weakly bound nanotubes (e.g., aerogels, bucky-papers) and rapid degradation. The large carbon fibers diameter is also beneficial as low surface area carbons are obtained, leading to high first cycle efficiency. Nitrogen doping, catalyst role, and the structural/graphitic dis/order in turn are found to affect in a complex way the cycling stability, yet influence on the charge transfer properties and the amount of lithium stored.

TABLE 2 The as-synthesized CNX1–CNX5 with different precursors

Sample	Synthesis precursors
CNX1	Benzylamine + Toluene
CNX2	Benzylamine + Urea
CNX3	Benzylamine + Pyridine
CNX4	Benzylamine + 1, 2-Dichlorobenzene (2.5% Ferrocene)
CNX5	Benzylamine + 1, 2-Dichlorobenzene (12% Ferrocene)

Abbreviation: CNX, carbon nanotube sponges.

3 | CONCLUSION

To summarize, nitrogen-doped CNX were synthesized by utilizing a method of AACVD in a bi-sprayer system at a temperature of 1020°C. BZ-toluene, BZ-urea, BZ-pyridine, BZ-1,2 -dichlorbenzene (2.5% ferrocene) and BZ-1,2 -dichlorbenzene (12% ferrocene) were used as carbon and nitrogen dopant sources. SEM, TGA, XPS, XRD and Raman spectroscopy were used to characterize the composition and morphology of prepared CNXs. When utilized as anodes for Li-ion storage, CNXs displayed differences in electrochemical performances, assigned to the chemical composition and defect nature of the nanotubes. The CNX prepared from 2-dichlorbenzene with 12 wt.% ferrocene as catalyst, displayed the highest specific capacity (223 mAh g^{-1}), highest first cycle efficiency (90%) and good retention of (99.3%) at a current density of 0.1C after 200 cycles. Other CNX, albeit with moderately lower performances, still display high storage capacities with also excellent cycling stability. These lithium storage performances being tested and repported in a practically relevant low working potential range of 0.01–1V (vs. Li). Furthermore, all CNXs exhibit an ultralow capacity decay of 0.021% per cycle. The electrochemical performances are attributed to the 3D interconnected tubular sponge morphology, hybrid graphitic-amorphous structure, as well as surface chemistry and doping.

4 | EXPERIMENTAL SECTION

4.1 | Methodology

N-doped CNT sponges (CNXs) were synthesized by AACVD in a bisprayer system feeding the reactor at 1020°C for 4 hours. The precursors (shown in Table 2) were composed of ferrocene (Sigma-Aldrich, 98%), thiophene (Sigma-Aldrich, 99%), ethanol (CTR scientific, 99.7%), combined with the following carbon and nitrogen precursors: benzylamine, toluene, urea, pyridine,

and 1,2-dichlorobenzene. The concentrations of ferrocene (2.5 wt.%) and thiophene (0.124 wt.%) were kept constant in the first four samples (CNX1, CNX2, CNX3, and CNX4, see Table 2). For CNX5, more ferrocene was added reaching a concentration of 12 wt.%.[44] In all experiments, one sprayer contained the solution of benzylamine-ethanol (1:1) whilst the second sprayer was loaded with the remaining precursors. Both sprayers were connected to a quartz tube through a Y-shape glass connecting adapter. A tubular furnace (Barnstead Thermolyne Model F21100) was then used to heat the quartz tube. A flow of 1.0 L min^{-1} Ar H$_2$$^{-1}$ (Infra, 95.5%) was kept for first sprayer, whereas 0.8 L min^{-1} of pure Ar was used in the second sprayer.

4.2 | Materials characterization

The microstructure and morphology of the samples were characterized by scanning electron microscopy (SEM, FEI-Helios Nanolab DualBeam 600 Microscopy). X-ray diffraction (XRD) patterns were collected using SmartLab X-ray diffraction (Rigaku Corp.), Cu-Kα radiation anode. Thermogravimetric analysis (TGA) was performed using alumina containers, with air analysis gas, at a heating rate of 10°C min^{-1} (Mettler Toledo TGA 3+ STARe System). Raman spectroscopy was performed using a Renishaw inVia confocal Raman microscopy with a laser wavelength of 532 nm. X-ray photoelectron spectroscopy (XPS) measurements were performed on PHI 5000 VersaProbe II.

4.3 | Electrochemical tests

The working electrodes were prepared by pressing CNX powder (binder and additive free electrodes) onto the coin cell case (CR2032, TOB New Energy). The active material mass loading was in the range of ~2 mg cm^{-2}. The half-cells consisted of CNXs as working electrode, with metallic Li foil (TOB New Energy) as counter and pseudo-reference electrode. Glassfiber (Whatman, GF/D) was used as the separator. 1 M LiPF$_6$ solution in a 1:1 (volume) mixture of ethylene carbonate and dimethyl carbonate (DoDoChem Co.) was used as electrolyte. All manipulations were performed in an Ar-filled glove box (less than 0.1 ppm water and oxygen content). Galvanostatic discharge (Li uptake) and charge (Li extraction) in the voltage range from 0.1 to 1 V versus Li/Li$^+$ tests were carried out at constant and various current densities using Neware battery test system. EIS measurements of CNXs electrodes were carried out on VersaSTAT 3 (AMETEK Scientific Instruments). The impedance spectra were obtained by applying a sine wave with an amplitude of 5.0 mV over the frequency range of 100 kHz to 0.01 Hz.

CONFLICT OF INTEREST

The authors declare that they have no conflict of interest.

DATA AVAILABILITY STATEMENT

The datasets generated and analysed during the current study are available from the corresponding author upon reasonable request.

ORCID

Alexandru Vlad https://orcid.org/0000-0002-0059-9119

REFERENCES

1. J. M. Tarascon, M. Armand, *Nature* **2001**, *414*, 359.
2. N. Nitta, F. Wu, J. T. Lee, G. Yushin, *Mater. Today* **2015**, *18*, 252.
3. Q. Zhu, J. Wang, X. Liu, N. Ebejer, D. Rambabu, A. Vlad, *Angew. Chem., Int. Ed.* **2020**, *59*, 16579.
4. M. Li, J. Lu, Z. Chen, K. Amine, *Adv. Mater.* **2018**, *30*, 1.
5. G. Cao, *Natl. Sci. Rev.* **2017**, *4*, 16.
6. J. Wang, A. E. Lakraychi, X. Liu, L. Sieuw, C. Morari, P. Poizot, A. Vlad, *Nat. Mater.* **2021**, *20*, 665.
7. A. Vlad, N. Singh, S. Melinte, J. F. Gohy, P. M. Ajayan, *Sci. Rep.* **2016**, *6*, 22194
8. S. W. Lee, N. Yabuuchi, B. M. Gallant, S. Chen, B.-S. Kim, P. T. Hammond, Y. Shao-Horn, *Nat. Nanotechnol.* **2010**, *5*, 531.
9. B. Ernould, O. Bertrand, A. Minoia, R. Lazzaroni, A. Vlad, J.-F. Gohy, *RSC Adv.* **2017**, *7*, 17301.
10. S. Chen, L. Qiu, H.-M. Cheng, *Chem. Rev.* **2020**, *120*, 2811.
11. J. Bourgeois, A. Vlad, S. Melinte, J. Gohy, *Chinese J. Chem.* **2017**, *35*, 41.
12. S. Zhong, H. Liu, D. Wei, J. Hu, H. Zhang, H. Hou, M. Peng, G. Zhang, H. Duan, *Chem. Eng. J.* **2020**, *395*, 125054.
13. J. Du, S. Gao, P. Shi, J. Fan, Q. Xu, Y. Min, *J. Power Sources* **2020**, *451*, 227727.
14. H. Jia, T. Quan, X. Liu, L. Bai, J. Wang, F. Boujioui, R. Ye, A. Vlad, Y. Lu, J.-F. Gohy, *Nano Energy* **2019**, *64*, 103949.
15. B. Lee, M. Kim, S. Kim, J. Nanda, S. J. Kwon, H. D. Jang, D. Mitlin, S. W. Lee, *Adv. Energy Mater.* **2020**, *10*, 1903280.
16. L. Cheng, X. Du, Y. Jiang, A. Vlad, *Nano Energy* **2017**, *41*, 193.
17. A. Vlad, N. Singh, C. Galande, P. M. Ajayan, *Adv. Energy Mater.* **2015**, *5*, 1402115.
18. B. Ernould, M. Devos, J.-P. Bourgeois, J. Rolland, A. Vlad, J.-F. Gohy, *J. Mater. Chem. A* **2015**, *3*, 8832.
19. H. Qu, J.-P. Bourgeois, J. Rolland, A. Vlad, J.-F. Gohy, M. Skorobogatiy, *Mater. Res. Soc. Symp. Proc.* **2013**, *1489*, 1.

20. A. E. Lakraychi, F. Dolhem, A. Vlad, M. Becuwe, *Adv. Energy Mater.* **2021**, *11* 2101562.

21. J. B. Goodenough, K.-S. Park, *J. Am. Chem. Soc.* **2013**, *135*, 1167.

22. Z. Chen, Q. Wang, K. Amine, *Electrochim. Acta* **2006**, *51*, 3890.

23. M. F. El-Kady, Y. Shao, R. B. Kaner, *Nat. Rev. Mater.* **2016**, *1*, 16033.

24. Y. P. Wu, E. Rahm, R. Holze, *J. Power Sources* **2003**, *114*, 228.

25. B. J. Landi, M. J. Ganter, C. D. Cress, R. A. DiLeo, R. P. Raffaelle, *Energy Environ. Sci.* **2009**, *2*, 638.

26. Y. Xu, C. Zhang, M. Zhou, Q. Fu, C. Zhao, M. Wu, Y. Lei, *Nat. Commun.* **2018**, *9*, 1720.

27. M. - F. Yu, O. Lourie, M. J. Dyer, K. Moloni, T. F. Kelly, R. S. Ruoff, *Science (80-.)* **2000**, *287*, 637 LP.

28. P. Sehrawat, C. Julien, S. S. Islam, *Mater. Sci. Eng. B* **2016**, *213*, 12.

29. C. de las Casas, W. Li, *J. Power Sources* **2012**, *208*, 74.

30. S. Nardecchia, D. Carriazo, M. L. Ferrer, M. C. Gutiérrez, F. del Monte, *Chem. Soc. Rev.* **2013**, *42*, 794.

31. X. Gui, J. Wei, K. Wang, A. Cao, H. Zhu, Y. Jia, Q. Shu, D. Wu, *Adv. Mater.* **2010**, *22*, 617.

32. Z. Lin, Z. Zeng, X. Gui, Z. Tang, M. Zou, A. Cao, *Adv. Energy Mater.* **2016**, *6*, 1600554.

33. A. J. Cortés-López, E. Muñoz-Sandoval, F. López-Urías, *Carbon (N.Y.)* **2018**, *135*, 145.

34. P. Sood, K. C. Kim, S. S. Jang, *ChemPhysChem* **2018**, *19*, 753.

35. P. Sood, K. C. Kim, S. S. Jang, *J. Energy Chem.* **2018**, *27*, 528.

36. F. López-Urías, R. Lv, H. Terrones, M. Terrones, *Graphene Chem.* **2013**, 183.

37. M. Crespo, M. González, A. L. Elías, L. Pulickal Rajukumar, J. Baselga, M. Terrones, J. Pozuelo, *Phys. Status Solidi RRL* **2014**, *8*, 698.

38. C. V. Rao, C. R. Cabrera, Y. Ishikawa, *J. Phys. Chem. Lett.* **2010**, *1*, 2622.

39. A. A. El Mel, A. Achour, W. Xu, C. H. Choi, E. Gautron, B. Angleraud, A. Granier, L. Le Brizoual, M. A. Djouadi, P. Y. Tessier, *Nanotechnology* **2011**, *22*, 435302.

40. H. Wang, C. Zhang, Z. Liu, L. Wang, P. Han, H. Xu, K. Zhang, S. Dong, J. Yao, G. Cui, *J. Mater. Chem.* **2011**, *21*, 5430.

41. R. Czerw, M. Terrones, J.-C. Charlier, X. Blase, B. Foley, R. Kamalakaran, N. Grobert, H. Terrones, D. Tekleab, P. M. Ajayan, W. Blau, M. Rühle, D. L. Carroll, *Nano Lett.* **2001**, *1*, 457.

42. M. Terrones, P. M. Ajayan, F. Banhart, X. Blase, D. L. Carroll, J. C. Charlier, R. Czerw, B. Foley, N. Grobert, R. Kamalakaran, P. Kohler-Redlich, M. Rühle, T. Seeger, H. Terrones, *Appl. Phys. A* **2002**, *74*, 355.

43. W. Chen, Z. Fan, X. Pan, X. Bao, *J. Am. Chem. Soc.* **2008**, *130*, 9414.

44. C. L. Rodríguez-Corvera, J. L. Fajardo-Díaz, A. J. Cortés-López, L. E. Jiménez-Ramírez, E. Muñoz-Sandoval, F. López-Urías, *Mater. Today Chem.* **2019**, *14*, 100200.

45. A. Aqil, A. Vlad, M. - L. Piedboeuf, M. Aqil, N. Job, S. Melinte, C. Detrembleur, C. Jérôme, *Chem. Commun.* **2015**, *51*, 9301.

46. D. C. Lee, F. V Mikulec, B. A. Korgel, *J. Am. Chem. Soc.* **2004**, *126*, 4951.

47. X. Lin, X. Lu, T. Huang, Z. Liu, A. Yu, *J. Power Sources* **2013**, *242*, 855.

48. E. Muñoz-Sandoval, A. J. Cortes-López, B. Flores-Gómez, J. L. Fajardo-Díaz, R. Sánchez-Salas, F. López-Urías, *Carbon (N.Y.)* **2017**, *115*, 409.

49. I. O. Maciel, N. Anderson, M. A. Pimenta, A. Hartschuh, H. Qian, M. Terrones, H. Terrones, J. Campos-Delgado, A. M. Rao, L. Novotny, A. Jorio, *Nat. Mater.* **2008**, *7*, 878.

50. K. N. Kudin, B. Ozbas, H. C. Schniepp, R. K. Prud'homme, I. A. Aksay, R. Car, *Nano Lett.* **2008**, *8*, 36.

51. G. Andrade-Espinosa, E. Munoz-Sandoval, M. Terrones, M. Endo, H. Terrones, J. R. Rangel-Mendez, *J. Chem. Technol. Biotechnol.* **2008**, *84*, 519.

52. J. L. Fajardo-Díaz, F. López-Urías, E. Muñoz-Sandoval, *Carbon (N.Y.)* **2020**, *164*, 324.

53. Y. Zhao, F. Yin, Y. Zhang, C. Zhang, A. Mentbayeva, N. Umirov, H. Xie, Z. Bakenov, *Nanoscale Res. Lett.* **2015**, *10*, 450.

54. B. Ernould, L. Sieuw, G. Barozzino-Consiglio, J.-F. Gohy, A. Vlad, *ACS Appl. Energy Mater.* **2019**, *2*, 7879.

55. J. O. Omale, R. Rupp, P. Van Velthem, V. Van Kerckhoven, V.-A. Antohe, A. Vlad, L. Piraux, *Energy Storage Mater.* **2019**, *21*, 77.

56. W. A. Schalkwijk, B. Scrosati, *Advances in Lithium-Ion Batteries*, Kluwer Academic Publishers **2015**.

SUPPORTING INFORMATION

Additional supporting information may be found in the online version of the article at the publisher's website.